Mechanics of Materials 151 (2020) 103603

Contents lists available at ScienceDirect

Mechanics of Materials

journal homepage: www.elsevier.com/locate/mechmat

Nanoscale modelling of combined isotropic and kinematic hardening of 6000 series aluminium alloys

Ole Runar Myhr [a,b], Tore Børvik [b,c], Calin D. Marioara [d], Sigurd Wenner [d], Odd Sture Hopperstad [b,c,*]

[a] Hydro Aluminium, Research and Technology Development, Sunndalsøra, Norway
[b] Structural Impact Laboratory (SIMLab), Department of Structural Engineering, NTNU – Norwegian University of Science and Technology, Trondheim, Norway
[c] Centre for Advanced Structural Analysis (CASA), NTNU, Trondheim, Norway
[d] Materials and Nanotechnology, SINTEF Industry, Trondheim, Norway

ARTICLE INFO

Keywords:
Bauschinger effect
Backstress
Hardening stagnation
Compression-tension tests
SEM
TEM

ABSTRACT

Kinematic hardening is incorporated into a nanoscale model for 6000 series aluminium alloys consisting of three sub-models describing in turn precipitation of hardening particles, yield strength and work hardening. The kinematic hardening model assumes that the backstress is caused by an unrelaxed plastic strain around non-shearable particles which is defined by an evolution equation. Compression-tension tests are performed on a cast and homogenized AA6063 aluminium alloy in tempers T6 (peak strength), T7 (overaged) and O (annealed). These tempers have different amounts of non-shearable hardening precipitates and thus exhibit various levels of kinematic hardening. The pre-compression is varied between 0.5% and 6% strain, after which the specimen is stretched to fracture. The grain structure, the constituent particles and the precipitate structure of the three tempers of the alloy are characterized by means of optical microscopy and scanning and transmission electron microscopy. The alloy displays marked kinematic hardening in all three tempers, whereas hardening stagnation is observed for tempers T7 and O. The proposed model captures the stress-strain response during strain reversal by means of the backstress and the storage and annihilation of geometrically necessary dislocations at the non-shearable particles.

1. Introduction

Aluminium alloys of the 6000 series find applications among others in energy absorbing automotive structural components such as bumper beams and crash boxes in the front and rear end of vehicles (Hirsch, 2011) and battery frames protecting the battery modules in electric cars (Scamans, 2018). In the event of a crash, the material in the protective structure will experience non-monotonic loading. For instance, a crash box undergoing axial folding will first be loaded in compression to substantial strains, before it buckles locally. Inside the local buckles, the material will typically experience continuing compression on one side of the wall and load reversal into tension on the other. Thus, on the tension side of the local buckle a strain path change takes place, which may significantly influence the subsequent material response under tensile loading. Even though the non-monotonic loading is of minor importance for the peak force and the energy absorption of the crash box (Langseth et al., 1999), it may be important for material failure. As aluminium is used in vehicles to reduce weight, the demand for optimized components often requires exploitation of the material to the verge of failure.

The aluminium alloys in the Al–Mg–Si(-Cu) (6000) series are age-hardenable (Polmear, 2005). Following casting, homogenization and some sort of forming operation such as rolling or extrusion, the material may be given a separate solution heat-treatment followed by either natural or artificial ageing, in which case metastable precipitates form. While the naturally aged material is strengthened by solute atoms and atomic clusters, the artificially aged material contains a high density of needle/rod/lath-shaped precipitate particles. They have one main coherency direction with the Al matrix along <100>Al, which coincides with the main precipitate growth direction. The precipitation sequence in Cu-free 6000-series alloys can be written as (Saito et al., 2018):

$$\text{SSSS} \rightarrow \text{Atomic clusters} \rightarrow \text{GP zones} \rightarrow \beta'' \rightarrow \beta', \text{U1}, \text{U2}, \text{B}' \rightarrow \beta - \text{Mg}_2\text{Si (stable)}$$

* Corresponding author. Structural Impact Laboratory (SIMLab), Department of Structural Engineering, NTNU – Norwegian University of Science and Technology, Trondheim, Norway.
E-mail address: odd.hopperstad@ntnu.no (O.S. Hopperstad).

https://doi.org/10.1016/j.mechmat.2020.103603
Received 18 March 2020; Received in revised form 17 September 2020; Accepted 17 September 2020
Available online 26 September 2020

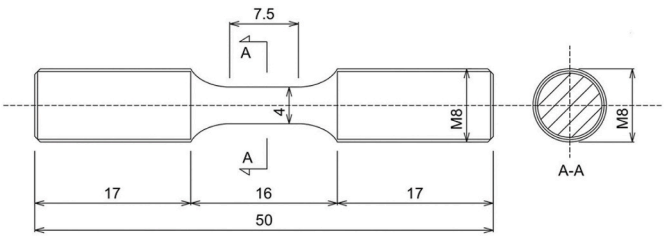

Fig. 1. Geometry of the axisymmetric test specimens.

where SSSS stands for super-saturated solid solution, i.e., the state of the material after rapid cooling from solution heat treatment. The metastable particles impede dislocation motion and strengthen the material. The most important phase in this respect is β'', found in most peak-hardness conditions. It dissolves and transforms upon prolonged artificial ageing and the next phases in the precipitation sequence nucleate. This process is associated with a decrease in the precipitate number density, an increase in precipitate size (needle length and cross-section) and a decrease in hardness.

In addition to the precipitate-forming elements Si and Mg, 6000 series alloys usually contain a significant amount of Fe. For alloys that are intended to be non-recrystallized after hot-forming processes like extrusion, Mn and sometimes Cr are added. During solidification these elements form large (micron-sized) constituent particles, which are also called primary particles, while dispersoids with sizes up to around 100 nm may form during homogenization. The latter type of particles play an important role in controlling grain size and texture by pinning the grain boundaries during the extrusion process. Under normal conditions the constituent particles and the dispersoids are of α-AlSi(Fe, Mn) type, and for alloys with low Mn content their most common composition is $Al_{50}Fe_{12}Si_7$ (Cooper, 1967). As this phase contains Si and is stable during further alloy processing, it is important to quantify it to be able to calculate the amount of Si available for the formation of hardening precipitates during artificial ageing.

The aim of the current study is to introduce kinematic hardening in the nanoscale model for 6000 series aluminium alloys proposed by Myhr et al. (2010). The nanoscale model, henceforth denoted NaMo, describes precipitation of hardening particles under natural and artificial ageing of the material and uses the results to estimate the yield strength and the work hardening under plastic straining. In the yield strength model, account is taken for the intrinsic strength of aluminium against dislocation glide and the strengthening by solute atoms, atomic clusters, precipitate particles and dislocations. The work hardening model has contributions from statistically stored dislocations (SSDs) as well as geometrically necessary dislocations (GNDs) induced by plastic deformation around particles that are not shearable by dislocations (Ashby, 1970). The nanoscale model has recently been extended to account for room temperature storage and cold deformation process stages (Myhr et al., 2015) and strain rate and temperature (Myhr et al., 2018) on the yield strength and work hardening. However, the latest version of the model does not take into account the backstress induced by the non-shearable particles in the material, neither the shielding effect of dislocation loops stored around particles when the direction of the loading is reversed (Fribourg et al., 2011).

In a material with non-shearable particles, dislocations surpass the particle by the Orowan mechanism, i.e., the passing dislocation leaves behind a dislocation loop around the particle and thus increases the dislocation density. The dislocations generated by the Orowan mechanism are said to be geometrically necessary (Ashby, 1970) and they contribute to the work hardening of the material. There is, however, a limit to the number of dislocations that can be stored around a particle of a given size because of the large stress generated inside the particle by the stored dislocation loops. The particle stress can be reduced by several mechanisms, for instance particle cracking or interfacial decohesion, or recovery mechanisms inhibiting further accumulation of dislocations around the particle (Proudhon et al., 2008). There are at least two effects of the non-shearable particles on the work hardening behaviour of the material: the storage of GNDs around the non-shearable particles that increases the dislocation density, and the existence of a backstress that evolves with plastic straining and leads to the Bauschinger effect (Brown and Stubbs, 1971a, 1971b). Another mechanism is the conceivable annihilation of Orowan loops around non-shearable particles by mobile dislocations with opposite Burgers vector travelling along the reversed path (Fribourg et al., 2011). When the load is reversed, the magnitude of the backstress and the density of GNDs first decrease to zero before starting to increase again with continued reversed loading.

The traditional way of investigating the influence of kinematic hardening on the material behaviour experimentally is to conduct strain reversal tests, for instance tension-compression tests or compression-tension tests on cylindrical specimens with relatively short gauge length to avoid buckling during compression (e.g. Fribourg et al. (2011), Proudhon et al. (2008), Kristoffersen et al. (2016), Qin et al. (2019)). Another possibility is to perform tension tests on cold rolled material, which allows for larger pre-strains than the compression-tension tests (e.g. Proudhon et al. (2008) and Qin et al. (2019)). In the current study, we perform compression-tension tests on short axisymmetric specimens on the aluminium alloy AA6063, which is one of the most common alloys used for extrusion. The alloy is heat-treated to three tempers, namely the peak strength condition (T6), a substantially overaged condition (T7) and the annealed condition (O), with different volume fractions of non-shearable particles. The strain level during pre-compression is varied between 0.5% and 6% to investigate the evolution of the backstress with plastic straining. Monotonic tension tests are conducted for comparison. Optical microscopy is used to map the grain structure and scanning and transmission electron microscopy (SEM and TEM) are used to characterize the constituent particles and the precipitate structure of the three tempers of the AA6063 alloy.

An extension of the nanoscale model NaMo for 6000 series aluminium alloys is proposed based on the obtained experimental dataset and existing models from the literature (Fribourg et al. (2011) and Proudhon et al. (2008)). In the enhanced version, an evolution equation for the backstress is included using the model proposed in Proudhon et al. (2008), and, in addition, the effect of shielding of particles during reversed loading is investigated following along the same line as described in Fribourg et al. (2011). The proposed work-hardening model has three internal variables: the density of statistically stored dislocations, the density of geometrically necessary dislocations, and the unrelaxed plastic strain responsible for the kinematic hardening. The results obtained by the augmented version of the nanoscale model NaMo are compared with the experimental data from the mechanical tests and the material characterization.

2. Experimental

2.1. Materials and processing

Axisymmetric specimens for compression-tension testing were machined from a homogenized extrusion billet of the aluminium alloy AA6063 with loading axis in the longitudinal direction of the billet. In the homogenization, the material was heated to 575 °C with a heating rate of 200 °C/h and held at this temperature for 2 h and 15 min before cooled to RT with a cooling rate of 400 °C/h. This corresponds to industrial practise. Specimen geometry is defined in Fig. 1 and the alloy composition is given in Table 1. The gauge region of the specimen has 4 mm diameter and 7.5 mm parallel length. The short parallel length is adopted to avoid buckling during the pre-compression of the specimen. The alloy is assumed to be nearly isotropic in the cast and homogenized condition, which has been verified for various aluminium alloys in e.g. Pedersen et al. (2015).

Table 1
Chemical composition of aluminium alloy AA6063 in wt% and at% in brackets.

Si	Mg	Fe	Mn	Ti	Zn	Cu	Cr	Al
0.512	0.470	0.206	0.047	0.0060	0.0030	0.001	0.001	Bal.
(0.492)	(0.522)	(0.010)	(0.023)	(0.0034)	(0.0012)	(0.0004)	(0.0005)	Bal.

Table 2
Artificial ageing.

Temper	Heating rate	Ageing temperature	Time at ageing temperature
T6	200°C/hour	185 °C	8 h
T7	200°C/hour	250 °C	10 h
O	200°C/hour	410 °C	4 h

The specimens were solution heat-treated at 560 °C for 10 min in a salt bath, water quenched, stored at room temperature for 24 h, and artificially aged to tempers T6, T7 and O using an air circulation oven, as specified in Table 2. The specimens were cooled in air after the artificial ageing.

Tensile tests to fracture were performed after 0%, 0.5%, 1%, 2%, 4% and 6% pre-compression, for each of the T6, T7 and O tempers. Two repeat tests were conducted to evaluate the consistency of the obtained stress-strain curves. The experiments were performed using a universal testing machine with a 250 kN load cell to apply the load and an AEROEL XLS 13XY laser micrometre to continuously measure the current diameter of the specimen (Fourmeau et al., 2013). To ensure that the minimum cross-section diameter was measured, the laser micrometre was adjusted along the gauge length of the specimen during testing. The true stress σ and the logarithmic (or true) strain ε were calculated according to

$$\sigma = \frac{F}{A}, \quad \varepsilon = \ln\frac{A_0}{A} + (1-2\nu)\frac{F}{EA} \tag{1}$$

where F is the force, E is Young's modulus, ν is Poisson's ratio, $A = \pi D_1 D_2/4$ and $A_0 = \pi D_0^2/4$ are the current and initial cross-section area, respectively, D_1 and D_2 are the two orthogonal diameters measured by the laser micrometre, and D_0 is the initial diameter of the specimen. The expression for the logarithmic strain is taken from Rakvåg et al. (2014). The plastic strain ε_p is calculated as

$$\varepsilon_p = \varepsilon - \varepsilon_e = \varepsilon - \frac{\sigma}{E} \tag{2}$$

where $\varepsilon_e = \sigma/E$ is the elastic strain. After diffuse necking, σ and ε represent average measurements of the true stress and the logarithmic strain over the minimum cross-section area of the specimen. The accumulated plastic strain p is calculated as

$$p = \int |d\varepsilon_p| \tag{3}$$

where $d\varepsilon_p$ is the plastic strain increment.

Fractured tensile test specimens with 6% pre-compression were used to prepare SEM and TEM samples as follows: for each temper, one set of samples was prepared from the undeformed head part of the fractured tensile test specimen, while another set was prepared from the area close to the fracture tip (that has been 6% pre-compressed and then stretched to fracture).

2.2. Scanning electron microscopy (SEM)

Samples of the undeformed material in the as-homogenized condition and after annealing to O temper were mechanically ground and polished with a diamond lapping film (grain size 1 μm). The distribution of the constituent particles in the as-homogenized condition was obtained by image processing of back-scattered electron micrographs taken in a Hitachi SU-6600 FESEM operated at 10 kV. A total of 29 images, which represent a total area of approximately 0.223 mm^2, were investigated to determine the area fraction of particles. The images contained 1320 constituent particles. The annealed samples were imaged with a FEI APREO FESEM operated at 10 kV, to measure the volume fraction of precipitated β-Mg_2Si particles. The particle volume fractions together with stoichiometric phase compositions were used to calculate the amount of Mg and Si left in solid solution after annealing.

Secondary electron SEM imaging was also conducted on the surface of electropolished TEM specimens prepared close to the fracture tip of the tensile sample to observe the 3D structure of β-Mg_2Si particles and estimate the number of particles that were fractured following compression-tension testing with 6% pre-compression.

The polished samples were anodized at room temperature for 2 min using HBF_4 to reveal the grain structure under polarized light in the optical microscope.

2.3. Transmission electron microscopy (TEM)

TEM specimens were prepared from the undeformed parts (heads) of the tensile test samples with 6% pre-compression, by cutting transversal sections of the specimens. In this way the TEM observation direction was along the longitudinal axis of the tensile test specimen. The cut slices were thinned down to around 100 μm, punched into 3 mm diameter discs, and electropolished with a TenuPol-5 machine using a mixture of 1/3 HNO_3 and 2/3 methanol kept at −25 °C and a voltage of 20 V.

Characterization of tempers T6, T7 and O was performed with a Jeol JEM-2100 TEM equipped with a LaB_6 filament and operated at 200 kV and used in bright field (BF) mode. Parameters of the hardening precipitates (number density, average needle cross-section, length and volume fraction) have been quantified following the methodology described in Marioara et al. (2005). A Gatan imaging filter (GIF), attached to the TEM instrument, was used for specimen thickness measurement. For each temper, between 500 and 550 needle lengths and between 200 and 250 needle cross-sections were measured to ensure good statistical accuracy. Between 2000 and 2300 precipitates were counted for each temper from eight to eleven images for the precipitate number density calculations.

3. Nanoscale model

NaMo is a nanoscale material model for 6000 series aluminium alloys with three interacting sub-models: a precipitation model, a yield strength model and a work hardening model (Myhr et al., 2010). The input to NaMo is the chemical composition of the alloy and the thermo-mechanical history after the rolling or extrusion process. The precipitation model calculates two different particle size distributions (PSDs) to represent the different types of precipitates and atomic clusters that tend to form in different temperature regions during thermo-mechanical processing, in addition to the mean solute concentration in the matrix (Myhr et al., 2015). The first PSD is for β'' and β' particles which are nucleated during artificial ageing, while the second PSD is for atomic clusters which form during natural ageing. The volume fraction of non-shearable precipitate particles (or Orowan particles) is also estimated based on a critical radius for cutting/looping of particles.

In the following, we will describe the extended version of NaMo in which kinematic hardening has been included. The changes only apply to the yield strength and work hardening models, whereas the

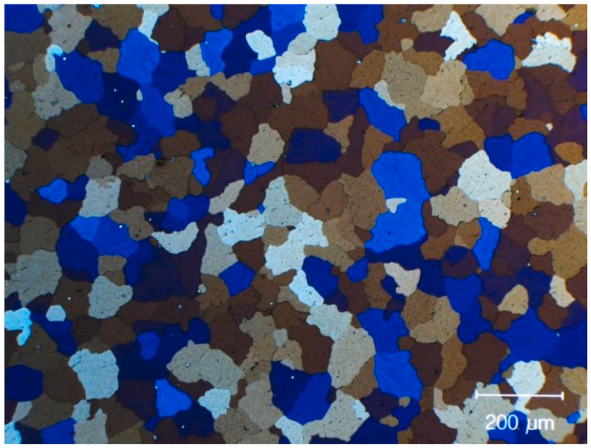

Fig. 2. Grain structure of cast and homogenized aluminium alloy AA6063.

(a)

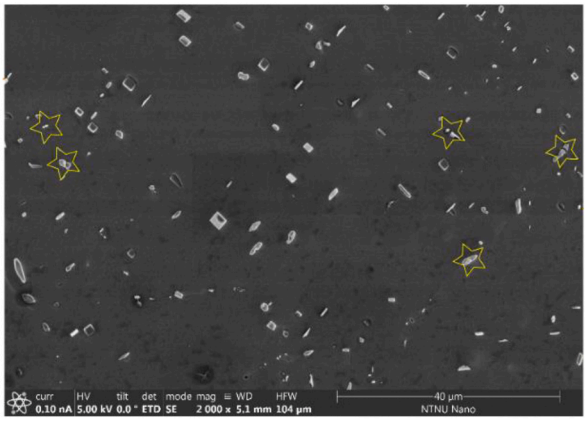

(b)

Fig. 3. SEM images showing the size and distribution of constituent particles in the AA6063 alloy: (a) Back-scattered image of undeformed O temper. Light particles are constituent α-$Al_{50}Fe_{12}Si_7$ and dark particles are β-Mg_2Si. (b) Secondary electron image of O temper close to the fracture of the tensile sample, in a material with 6% pre-compression. The stars encompass fractured particles.

precipitation model as described in Myhr et al. (2015) is left unchanged.

The yield criterion is expressed as

$$f \equiv |\sigma - \sigma_b| - \sigma_y = 0 \tag{4}$$

where σ is the stress and σ_b is the backstress. The backstress is expressed as (Fribourg et al., 2011)

$$\sigma_b = f_O E_p \varepsilon_p^* \tag{5}$$

where f_O is the volume fraction of Orowan particles, E_p is the elastic modulus of these particles, and ε_p^* is the unrelaxed plastic strain, which is closely related to the density of GNDs, as will be explained later in this section. The microstructural parameter f_O is estimated by the precipitation model of NaMo (Myhr et al., 2010). Based on Fribourg et al. (2011) and Proudhon et al. (2008), the evolution of the unrelaxed plastic strain is defined by

$$d\varepsilon_p^* = d\varepsilon_p - \frac{\varepsilon_p^*}{\varepsilon_c} dp \tag{6}$$

where $d\varepsilon_p = \vartheta dp$ with $dp \geq 0$, $\vartheta = \mathrm{sgn}(\sigma - \sigma_b)$ defines the loading direction, and ε_c is the saturation value of $\left|\varepsilon_p^*\right|$. We will assume here that the maximum number of storage sites around a particle scales with the particle radius, so that ε_c can be considered constant. Assuming initial values ε_{p0}^* and ε_{p0} of the unrelaxed plastic strain and the plastic strain, respectively, integration of this differential equation during a half-cycle gives the unrelaxed plastic strain as

$$\varepsilon_p^*(\varepsilon_p) = \vartheta\varepsilon_c + \left(\varepsilon_{p0}^* - \vartheta\varepsilon_c\right)\exp\left[-\frac{\vartheta}{\varepsilon_c}\left(\varepsilon_p - \varepsilon_{p0}\right)\right] \tag{7}$$

where it is evident that $\varepsilon_p^* \to \vartheta\varepsilon_c$ when $\vartheta\varepsilon_p \to \infty$. The critical plastic strain for saturation of GNDs, ε_c, is given as (Myhr et al., 2010)

$$\varepsilon_c = \frac{f_O^r}{f_O}\varepsilon_c^r \tag{8}$$

where ε_c^r is the critical plastic strain for a reference alloy, and f_O and f_O^r are the volume fraction of non-shearable particles for a given alloy and a reference alloy, respectively.

The size of the elastic domain σ_y is defined by

$$\sigma_y = \sigma_i + \sigma_p + \sigma_{ss} + \sigma_d \tag{9}$$

where σ_i is the intrinsic yield stress of pure aluminium, σ_p is the contribution from atomic clusters and β'' and β' particles, σ_{ss} is the contribution from solute atoms, and σ_d is the contribution from dislocations. The justification of using linear addition for the strength contributions, as described by Equation (9), relies solely on the fact that this simple law seems to work well for the present type of alloys and heat treatment schedules (Myhr et al., 2010, 2015, 2018). Depending on the actual mixture of obstacles of various strength that oppose the dislocation movement, other addition laws, including Pythagorean addition, may sometimes be more realistic. The importance of how to add the strength contributions is confirmed by Kocks (1979), where the resulting stress-strain curves are significantly changed when switching from linear to Pythagorean addition.

Based on dislocation mechanics and estimated interaction forces between dislocations and obstacles, σ_p is calculated using parameters extracted from two individual PSDs (Myhr et al., 2015). One PSD represents atomic clusters, and the other β'' and β' particles. Here, only the PSD from β'' and β' particles is considered since the clusters are unstable at elevated temperatures and are expected to be completely dissolved after the heat treatments applied in the present work (Myhr et al., 2015). The strength contribution σ_p is then given as follows (Deschamps and Brechet, 1999)

$$\sigma_p = \frac{M\overline{F}}{bl} \tag{10}$$

where $\overline{F}$ is the mean obstacle strength and l is the effective particle

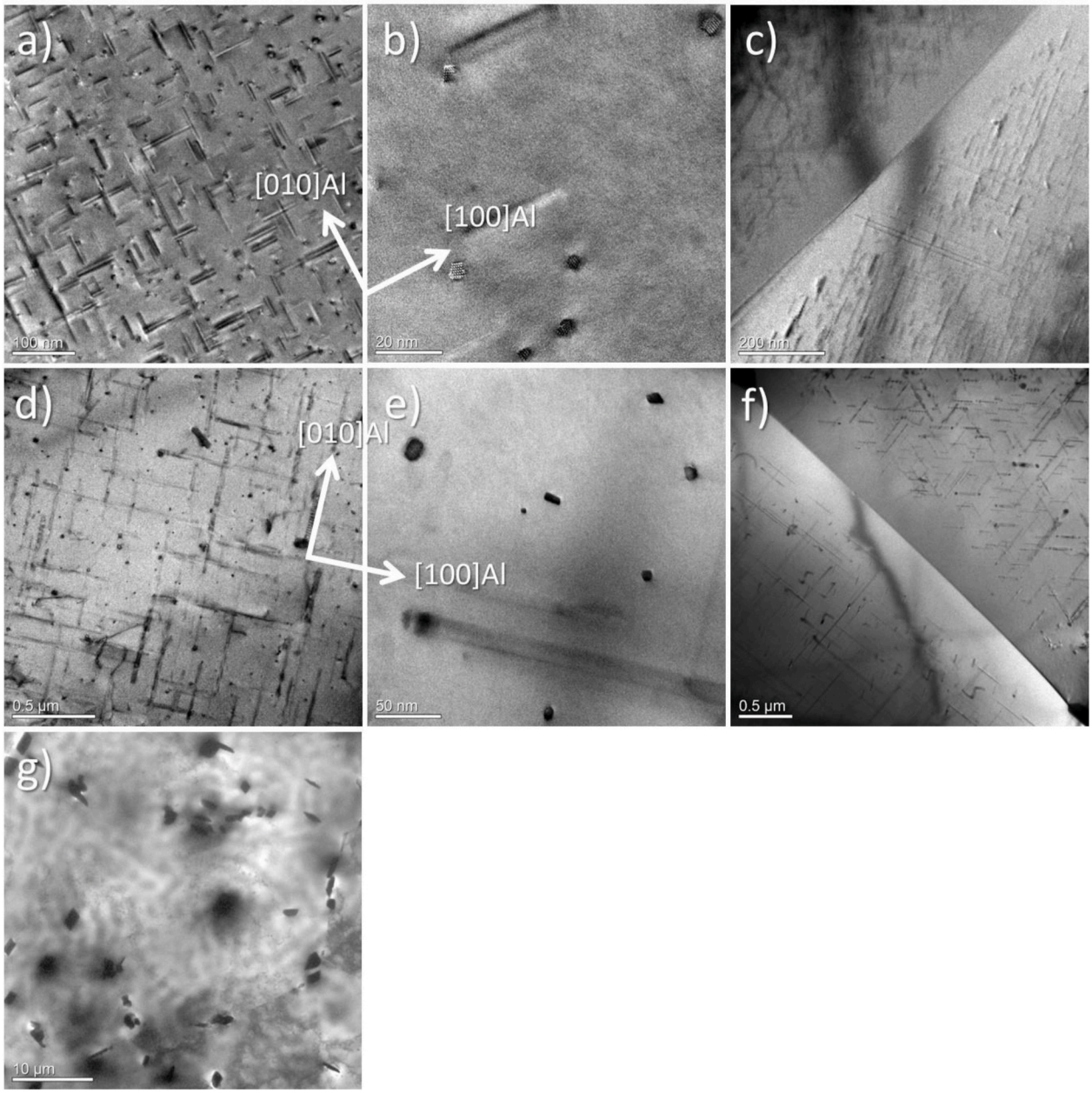

Fig. 4. TEM images of undeformed samples showing the size and distribution of precipitate particles for the three tempers T6 (a–c), T7 (d–f) and O (g). High angle grain boundaries and precipitation free zones are also shown in (c) and (f).

Table 3
Experimental data for precipitate particles. The data have been obtained from TEM for tempers T6 and T7, and from SEM for temper O. N_v is the average precipitate number density, l is the average precipitate needle length, A is the average precipitate cross-section, f is the precipitate volume fraction, C_{Si} is the calculated Si amount left in solid solution (in-between the needles), C_{Mg} is the corresponding Mg amount, and w_{PFZ} is the width of the precipitation free zone (PFZ) at the grain boundaries. Concentrations are given in wt% and at% in brackets.

Temper	N_v (#/µm^3)	l (nm)	A (nm^2)	f	C_{Si} (wt%)	C_{Mg} (wt%)	w_{PFZ} (nm)
T6	15,446	36.14	13.06	0.00730	0.156	0.214	~145
	±1626	±0.84	±0.35	±0.0008	(0.150)	(0.238)	
T7	298	354.43	69.02	0.00728	0.218	0.105	~600
	±36	±20.42	±5.35	±0.0011	(0.209)	(0.117)	
O	0.014 (*)	–	–	0.0053	0.309	0.224	–
	±0.002			±0.0005	(0.297)	(0.249)	

(*) Rough estimate based on the volume fraction given in the table, and an observed mean volume of the β-particles of 0.37 µm^3.

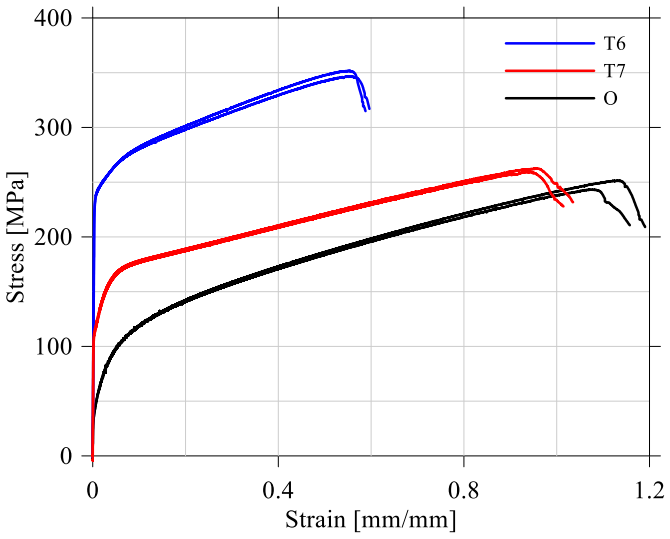

Fig. 5. True stress-strain curves in tension without pre-compression. The results from two repeat tests are shown for each temper and the curves are plotted to fracture.

spacing in the slip plane of the dislocation line. These two quantities are calculated from the PSD, while M is the Taylor factor and b is the magnitude of the Burgers vector.

The PSD for β'' and β' particles may contain a mixture of shearable and non-shearable precipitates with strength contributions corresponding to σ_p^s and σ_p^{ns}, respectively. The strength contribution σ_p^s is assumed to be unaffected by the loading direction. This contrasts with σ_p^{ns} for which the magnitude is assumed to change during reversed straining according to the mechanism described in Fribourg et al. (2011), and this approach is adopted in the present work. It is assumed that the Orowan loops stored around non-shearable precipitates during pre-straining are annihilated by the mobile dislocations with opposite Burgers vector when the loading direction is reversed. The non-shearable precipitates are here assumed to be "transparent" to the mobile dislocations and do not contribute to the flow stress during the first part of the reversed loading when the moving dislocations annihilate the loops. In the model, this effect is accounted for by multiplying σ_p^{ns} with a correction factor χ, which accounts for the shielding of the non-shearable particles by GNDs during reversed straining. Hence, σ_p can be expressed as follows

$$\sigma_p = \sigma_p^s + \chi\sigma_p^{ns} \tag{11}$$

The factor χ is here defined by

$$\chi = \begin{cases} 1 & \text{for} \quad \mathrm{sgn}\left(d\varepsilon_p^*\right) = \mathrm{sgn}\left(\varepsilon_p^*\right) \\ \left(1 - \left|\dfrac{\varepsilon_p^*}{\varepsilon_{max}}\right|\right)^q & \text{for} \quad \mathrm{sgn}\left(d\varepsilon_p^*\right) \neq \mathrm{sgn}\left(\varepsilon_p^*\right) \end{cases} \tag{12}$$

where ε_{max} is the maximum value of $\left|\varepsilon_p^*\right|$ during pre-compression The constant q has been estimated to 0.25 as a best-fit value from comparison between modelling results and experimental data. The factor χ equals unity when ε_p^* and $d\varepsilon_p^*$ have the same sign, which implies continuous straining in either tension or compression. If ε_p^* and $d\varepsilon_p^*$ have opposite signs (i.e., a strain reversal has occurred), χ is between zero and unity, and varies nonlinearly with ε_p^* from zero when $\left|\varepsilon_p^*/\varepsilon_{max}\right| = 1$ to unity when $\left|\varepsilon_p^*/\varepsilon_{max}\right| = 0$.

The solid solution hardening is given by the relation

$$\sigma_{ss} = \sum_i k_i C_i^{2/3} \tag{13}$$

where C_i is the concentration of a specific element in solid solution, and k_i is a scaling factor determining the strengthening effect of the relevant elements, here Mg and Si.

The dislocation strengthening σ_d is defined by the Taylor equation

$$\sigma_d = \alpha M \mu b \sqrt{\rho_s + \rho_g} \tag{14}$$

where μ is the shear modulus and α is a numerical constant. The evolution of the density of statistically stored dislocations with the plastic straining is defined by the Kocks-Mecking equation (Kocks and Mecking, 2003)

$$d\rho_s = \left(k_1\sqrt{\rho_s} - k_2\rho_s\right)dp \tag{15}$$

The parameter k_1 controls storage of dislocations and is constant for a class of alloys, whereas k_2 governs the dynamic recovery mechanism and depends on an effective solid solution concentration (Myhr et al., 2010). The density of geometrically necessary dislocations is defined by

$$\rho_g = \frac{k_g}{\lambda_g}\left|\varepsilon_p^*\right| \tag{16}$$

where k_g is a material parameter. The storage of geometrically necessary dislocations depends on the magnitude of the geometric slip distance λ_g, according to the Ashby formalism (Ashby, 1970), which is calculated from the PSD representing the hardening precipitates (Myhr et al., 2010). To calculate λ_g, a critical particle radius r_c above which dislocations bypass the particle by the Orowan mechanism must be defined.

The reader is referred to Myhr et al. (2010, 2015, 2018) for a more detailed description of the various parts of NaMo.

4. Experimental results

4.1. Grain structure and constituent particles

The grain structure after casting and homogenization is shown in Fig. 2. The mean grain size was estimated to 63 μm using the linear intercept method and measuring about 300 grains. The grain structure is not affected by the artificial ageing.

In cast and homogenized aluminium alloys, the large constituent particles are mainly observed on the grain boundaries and in the interdendritic regions (Westermann et al., 2014). The volume fraction of α-$Al_{50}Fe_{12}Si_7$ particles was estimated to 0.0050 after homogenization. Consequently, this phase incorporates 0.058 at% Si from the alloy composition. The distribution and size of the α-phase will not change significantly during the heat treatments, so this number will be used in solute calculations for all three temper conditions. The measured average size of the α-phase corresponds to an equivalent diameter of 1.11 μm.

The α-$Al_{50}Fe_{12}Si_7$ and β-Mg_2Si particles found in alloy AA6063 in O temper are illustrated in Fig. 3 (a). The volume fraction of β-Mg_2Si phase was estimated to 0.0053 in the O temper, which was calculated to absorb 0.137 at% Si and 0.273 at% Mg. Therefore, for the O temper, 0.297 at% Si and 0.249 at% Mg are left in solid solution and will contribute to solute hardening.

Fig. 3 (b) shows a SEM image of the sample in O temper that has been deformed to fracture in tension after 6% pre-compression. The image is taken from the area close to the fracture surface. The surface is electropolished, which removes the matrix and α-particles while the non-metallic β-Mg_2Si particles are kept intact, revealing their 3D shapes. The stars encircle β-Mg_2Si particles that seem to have fractured during the deformation, encompassing only about 1–2% of the particles. In the undeformed condition, no fractured particles were found.

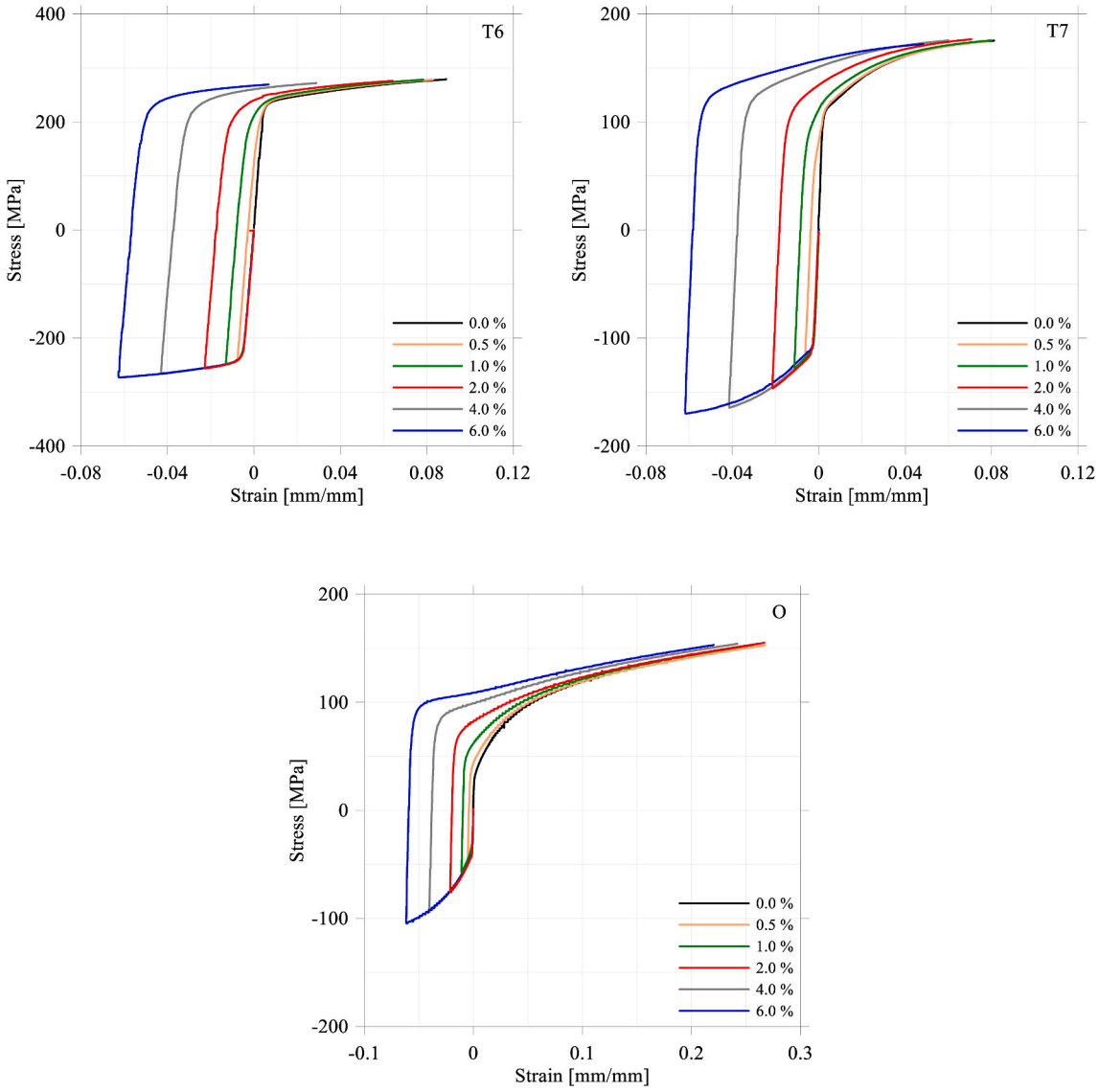

Fig. 6. True stress versus logarithmic strain curves from reversed tests on AA6063 in tempers T6, T7 and O plotted to incipient necking.

Particle fracture has been observed in similar type of alloys subjected to large plastic strains (Proudhon et al., 2008). In the present work, particle fracture was uncommon, so it seems unlikely that this mechanism plays an important role for the combination of alloy composition, temper conditions and reversed loading conditions used in the present investigation. Hence, the particle fracture mechanism has not been included in the present modelling. Grain boundaries represent another possible contribution to kinematic hardening which becomes important as the grain size decreases (Bardel et al., 2015). In the present work the grain boundaries were ignored with respect to kinematic hardening due to the large grain size of the material.

4.2. Precipitate structures observed in TEM

Fig. 4 shows TEM micrographs of the precipitate structure for undeformed materials in the three tempers T6, T7 and O, and precipitate free zones for the T6 and T7 tempers. Images such as (a) and (d) have been used for the measurement of needle lengths and calculation of precipitate volume density, while measurements of precipitate cross-sections were extracted from higher magnification images such as shown in (b) and (e). Based on the periodicities, shapes and orientations of precipitate cross-sections present in the latter type of images, it was concluded that the β'' metastable phase was dominant in the T6 temper, and β' in the T7 temper. However, U-phases and B′ have also been observed in the T7 temper. The particles are significantly smaller and the number density is larger for temper T6 than for temper T7. In the O temper, the equilibrium β-Mg_2Si phase is the only precipitate observed in significant amounts. These large particles are not elongated but are more equiaxed as compared with β'' and β' type of particles. Table 3 summarizes the precipitate parameters obtained from a statistical analysis of the precipitate structures as exemplified in Fig. 4.

The estimation of Mg and Si solutes bound to precipitates in the T6 temper was conducted by assuming that all precipitates contributing to the measured volume fraction are β'' with an equal mix of Mg_5Si_6, $Mg_5Al_2Si_4$ and $Mg_4Al_3Si_4$ compositions (Hasting et al., 2009). When taking into account that 22 atoms in β'' occupy the space of 24 atoms in fcc-Al, this means that the 0.730% volume fraction of β'' (cf. Table 3) incorporates 0.284 at% Mg and 0.284 at% Si from the alloy composition.

For the T7 temper, the calculation of Mg and Si solute bound to precipitates assumes that all precipitates are β' with composition Mg_9Si_5 (Vissers et al., 2007). In this case 28 atoms in β' occupy the volume of 32.4 atoms in fcc-Al. This means that the 0.728% volume fraction of β' (cf. Table 3) incorporates 0.405 at% Mg and 0.225 at% Si. However,

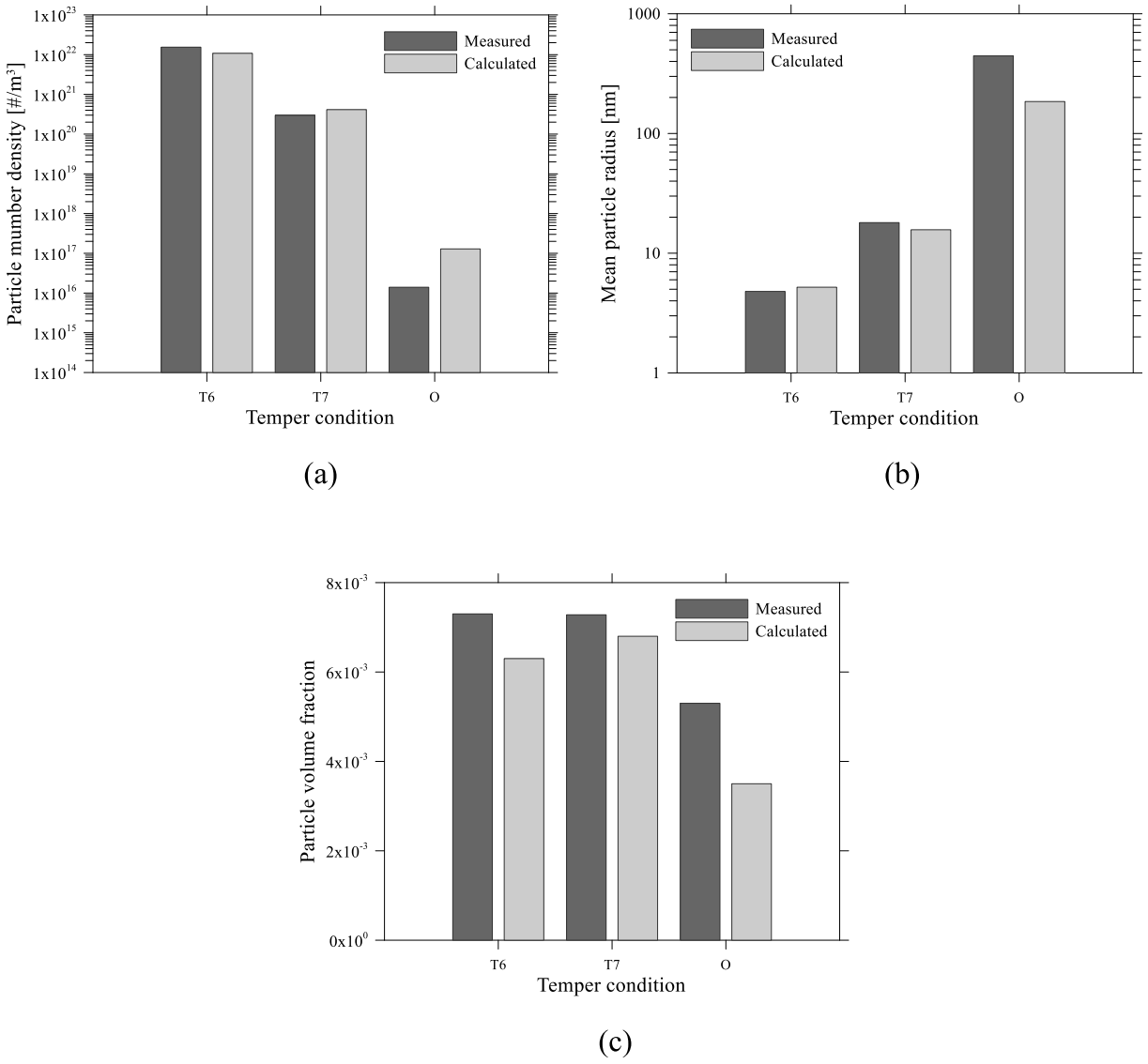

Fig. 7. Calculated precipitate parameters after ageing of alloy AA6063 to the temper conditions T6, T7 and O: (a) particle number density, (b) mean particle radius and (c) particle volume fraction.

because of the presence of U-phases and B′ with more Si-rich compositions than β', it is expected that the amount of Mg in precipitates is slightly lower than estimated above, and the amount of Si is consequently slightly higher.

Based on the above considerations, the amount of Mg and Si left in solid solution can be calculated, and the numbers are included in Table 3. For the O temper, the precipitate statistics in Table 3 is rough and just expected to give an order-of-magnitude estimate of the particle number density of the large equilibrium β-particles.

4.3. Tensile test results

The results of the monotonic tensile tests (i.e., with 0% pre-compression) are displayed in Fig. 5 in terms of the true stress-strain curves to fracture. Results from two repeat tests are plotted per temper and it is evident that the scatter between repeat tests is small. Temper T6 has a high number density of hardening precipitates and low solute level, giving the high strength and moderate work hardening rate. Temper T7 has intermediate strength and high initial work hardening rate which saturates at low strain. This behaviour is caused by storage of GNDs around non-shearable β' precipitates (Teichmann et al., 2013). Temper O has low strength and high work hardening rate, where the low strength is caused by a low number density of large β-Mg_2Si precipitates, and the high work hardening rate results from a significant number of atoms left in solid solution (Table 3). Temper T6 has a high number density of hardening precipitates and low solute level, giving the high strength and low work hardening rate. Temper T7 has intermediate strength and high initial work hardening rate which saturates at low strain. This behaviour is caused by storage of GNDs around non-shearable β' precipitates (Teichmann et al., 2013). Temper O has low strength and high work hardening rate, where the low strength is caused by a low number density of large β-Mg_2Si precipitates, and the high work hardening rate results from a significant number of atoms left in solid solution (Table 3).

The results from the reversal tests are presented in Fig. 6 and Fig. 12 for tempers T6, T7 and O. Fig. 6 presents the true stress-strain curves as measured during the tests, while Fig. 12 displays a comparison of the stress magnitude against the accumulated plastic strain between calculations (left) and measurements (right) for the reversed loading. Fig. 12 will be further discussed in Section 5.3. From the experimental data it appears that the strength of the materials tends to be somewhat higher in compression than in tension, i.e., there are signs of the strength

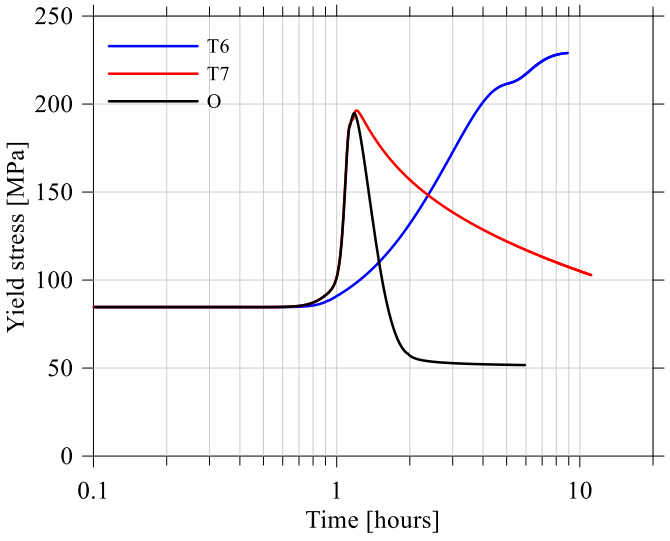

(a)

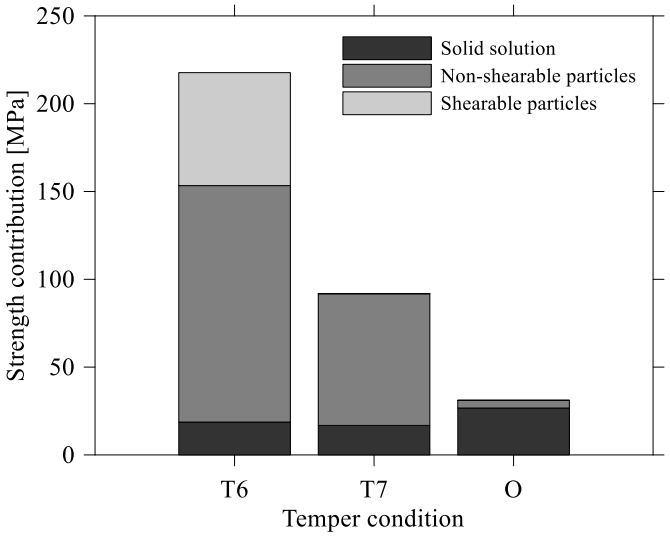

(b)

Fig. 8. (a) Calculated isotropic yield stress during ageing of alloy AA6063 alloy to the temper conditions T6, T7 and O. The time axis is from the start of the heating stage. (b) Strength contributions at the end of each heat treatment corresponding to the T6, T7 and O tempers. Note that the intrinsic yield stress contribution of pure aluminium, σ_i, is not included in (b).

differential effect, which has recently been studied experimentally for 6000 series aluminium alloys in Holmen et al. (2017). The Bauschinger effect is evident for the T6 temper after load reversal. In temper T7, the Bauschinger effect is strong, and the transient phase of elevated work hardening rate is longer than in temper T6. Hardening stagnation is observed for the two highest levels of pre-compression for temper T7. In temper O, the Bauschinger effect is weaker than in temper T7, but hardening stagnation is also seen for this temper for the two highest levels of pre-compression. Another phenomenon observed for temper O is serrated yielding, or the Portevin-Le Chatelier (PLC) effect, which is due to interaction between solute atoms and dislocations (e.g. Lademo et al. (2012)). Serrated yielding is observed both in the tension test and in the reversed loading tests. The reason for finding the PLC effect in temper O and not in tempers T6 and T7, is that the concentration of solid solution atoms is higher in this temper than in the two others. In all three tempers, there is some evidence of permanent softening or at least softening after load reversal that persists until necking, which is most clearly seen in Fig. 12.

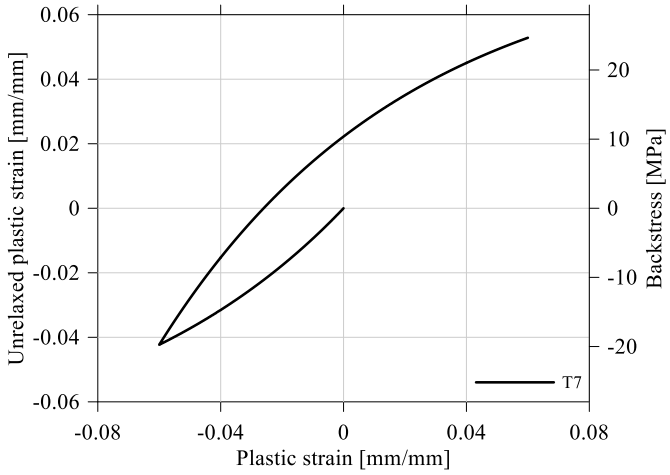

Fig. 9. Calculated evolution of the unrelaxed plastic strain and the resulting backstress during simulations of reversed loading of AA6063 in temper T7 for a pre-compression of 0.06. The following parameters have been used: $\varepsilon^*_{p0} = 0$, $\varepsilon_{p0} = 0$, and $\varepsilon_c = 0.080$.

5. Modelling results and validation

5.1. Precipitation model

The precipitation parameters calculated by NaMo form the basis for predictions of the isotropic yield stress and work hardening rate as well as the kinematic hardening response during reversed loading. The precipitation model has been validated in several works where modelling results have been compared to statistical precipitation data obtained from TEM (Myhr et al., 2001, 2015), and data for the atomic cluster distribution obtained by atom probe tomography analyses (Myhr et al., 2015). In the present work, the chemical composition of the alloy and the temperature history corresponding to each of the three tempers were used as input to the model. For all other input parameters, default data given in (Myhr et al., 2001, 2010, 2015) were used, and the simulations were run without any tuning or calibration.

The results are shown in Fig. 7 and summarized in Table 4. The calculated parameters can be compared to the experimentally obtained parameters compiled in Table 3. As NaMo does not take into consideration precipitate shapes for the needles formed in the T6 and T7 tempers, only the radius of an equivalent average precipitate volume ($\bar{r}$) is displayed in Table 4. Fig. 7(a), (b) and (c) show the experimentally measured and the calculated values for precipitate number density, mean particle radius and the particle volume fraction, respectively, for the three temper conditions. The measured particle number density is about 50 times larger for T6 than for T7, and T7 contains about 20,000 times more particles per volume than the O temper. The calculated mean particle radius varies as 5.2 nm, 15.7 nm and 185 nm going from T6 to T7 and O temper, while the corresponding figures from the measurements are 4.8 nm, 18 nm and 445 nm, respectively. The predicted volume fraction of particles shown in Fig. 7 (c) is 0.0063, 0.0068 and 0.0035 for T6, T7 and O, respectively, whereas the corresponding measurements give 0.0073, 0.0073 and 0.0053. For the T6 temper, the calculated volume fractions of shearable and non-shearable particles are 0.0020 and 0.0043, respectively. For the T7 and O tempers, all particles are non-shearable. The relatively small volume fraction of particles for the O temper is caused by the high solubility of Mg and Si at the ageing temperature of 410°C.

It is evident that the overall agreement between simulation results and measurements in Fig. 7 is reasonably good for all three temper conditions when taking into consideration that no tuning or calibration

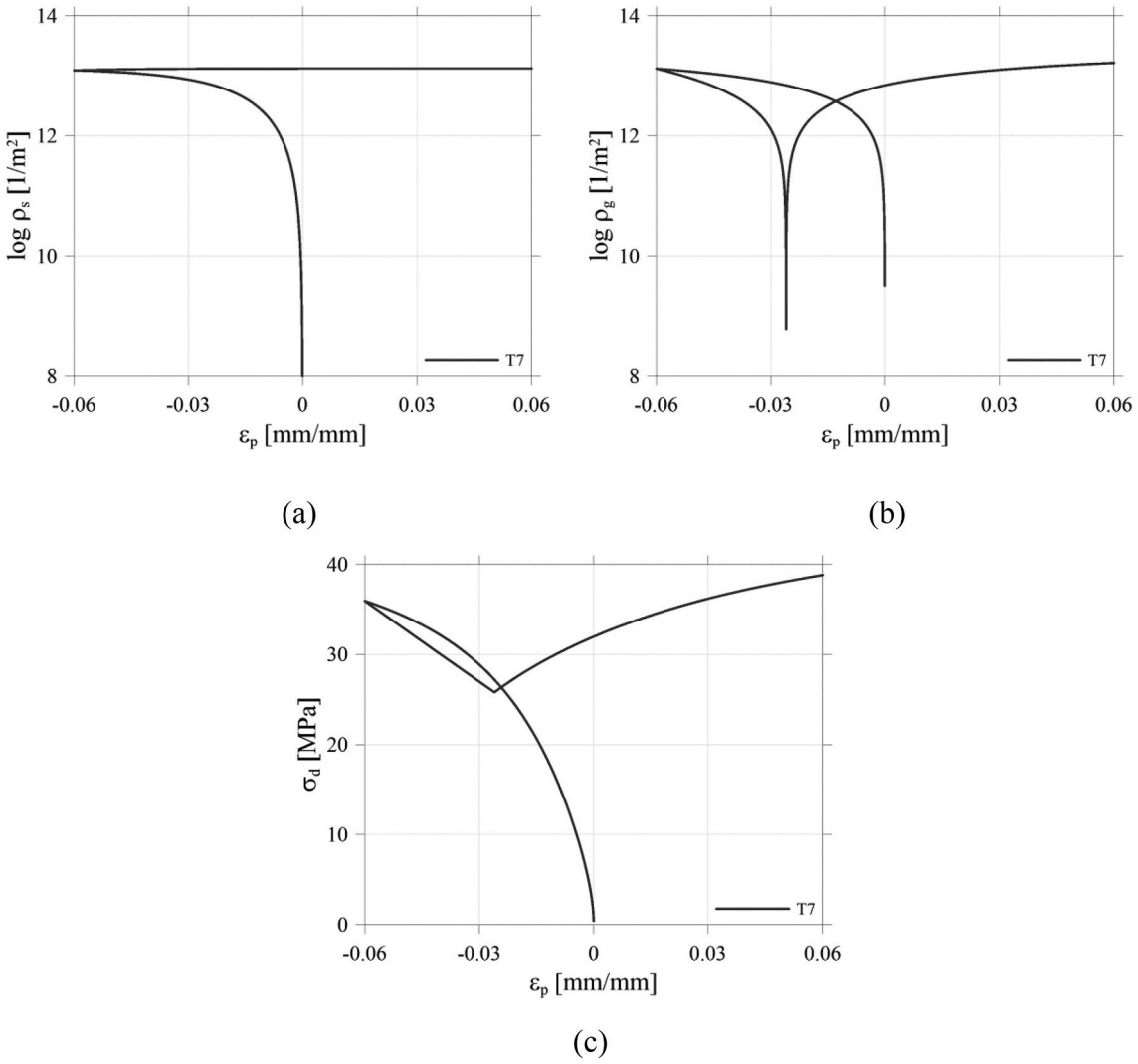

Fig. 10. Simulation results showing the evolution of the density of (a) statistically stored dislocations ρ_s, (b) geometrically necessary dislocations ρ_g, and (c) resulting flow stress from dislocations σ_d during reversed loading of AA6063 in temper T7 for a pre-compression of 0.06.

has been done. This is encouraging since reasonably accurate predictions of the precipitate structure is a prerequisite for confident use of the outputs from the precipitation model as inputs to the dislocation-based mechanical models as has been done in the following simulations.

5.2. Isotropic hardening model

Fig. 8 (a) displays the evolution of the isotropic yield strength for the three temper conditions during the final ageing heat treatment which follows the initial solution heat treatment and subsequent room temperature storage. The figure shows that these three ageing heat treatments give very different evolution of the yield strength. All three curves start at the same value of 85 MPa before the heating starts. The yield strength curve for the T6 temper increases slowly compared with the two other curves since the temperature is lower than for the T7 and O tempers, and the kinetics is correspondingly slow due to low diffusion rates. As can be seen from Fig. 8 (b), non-shearable particles are the main contribution to the strength of the T6 temper, but there is also a significant contribution from shearable particles. Solid solution hardening is low since most of the available solute atoms in terms of Mg and Si are tied up in particles. Fig. 8 (a) shows that for the T7 temper, the yield strength is close to the maximum value after the initial heating from room temperature to the ageing temperature of 250 °C. After about 1 h and 10 min, the yield strength starts to drop due to coarsening of the particles. The final yield strength at the end of the T7 heat treatment is only about 100 MPa. From Fig. 8 (b), the main yield strength contribution is from non-shearable particles. For the O temper, Fig. 8 (a) shows that the yield strength drops to about 50 MPa already during the heating stage, which takes about 2 h for this temper. The yield stress does not drop significantly during the holding at 410 °C since the solid solution concentrations of Mg and Si are close to the equilibrium value already after the heating cycle. At the same time, Fig. 7 (b) shows that the particles have grown to be very large at the end of the ageing at this high ageing temperature, and the strength contribution from particles is therefore low. Fig. 8 (b) shows that the main yield strength contribution for the O temper is from elements in solid solution.

The present version of NaMo does not account for phase transformations and assumes that the composition of the particles is Mg_5Si_6 irrespectively of alloy composition and heat treatment schedule that have been applied. This simplification gives slightly inaccurate predictions of the solid solution concentrations of Mg and Si, which is one of the reasons for the differences in C_{Si} and C_{Mg} in Tables 3 and 4. This inaccuracy in predictions of solid solution concentrations gives a corresponding inaccuracy in prediction of the strength contributions σ_{ss} in Equation (13). An estimate of the magnitude of this inaccuracy indicates a maximum of about 5 MPa for σ_{ss} for the T7 and O tempers. For the T6 temper, the assumed stoichiometry of the particles is probably close to the real composition, and the error is expected to be small.

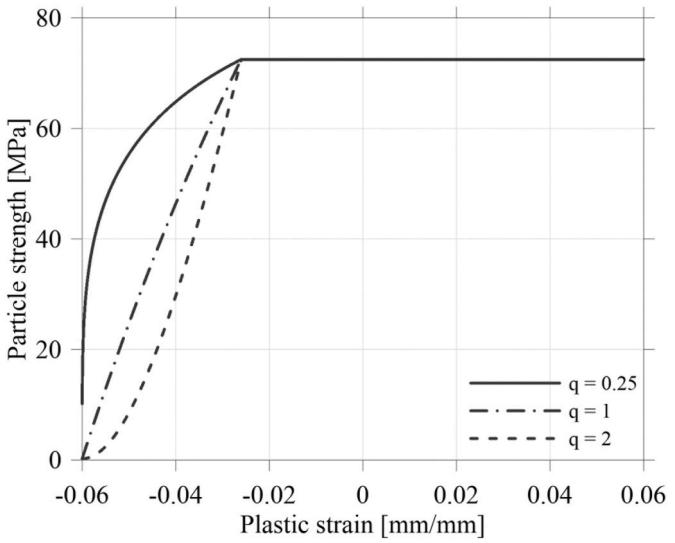

Fig. 11. Effect of exponent q in the expression for shielding of particles by geometrically necessary dislocations on resulting particle strength contribution σ_p. The present example relates to reversed loading for alloy AA6063 in temper T7, after a pre-compression of 0.06.

5.3. Kinematic hardening model

The new features of the extended NaMo model with kinematic hardening will now be presented through a modelling example related to the present AA6063 alloy in temper T7 subjected to compression-tension loading like the experiments described in Section 4.3.

The first step is to calculate the unrelaxed plastic strain ε_p^* for the actual loading case using the differential equation given by Equation (6), or the integrated version given by Equation (7). Fig. 9 shows the results from such a calculation for a pre-compression of 0.06, and with $\varepsilon_{p0}^* = 0$, $\varepsilon_{p0} = 0$, and $\varepsilon_c = 0.080$. The latter parameter is obtained from Equation (8) with $f_O = 0.0068$, $f_O^r = 0.0109$ (Myhr et al., 2010) and $\varepsilon_c^r = 0.05$ (Myhr et al., 2010). Fig. 9 also shows the evolution of the backstress σ_b, which according to Equation (5) is proportional to the unrelaxed plastic strain ε_p^*. The maximum backstress is about 20 and 25 MPa in compression and tension, respectively, which is based on a reported elastic modulus E_p for $\beta''(Mg_5Si_6)$ type of particles of 67 GPa (Yu et al., 2010). This value is somewhat uncertain, because the main type of particles is expected to be $\beta'(Mg_9Si_5)$ in the T7 condition, and these particles may have a different elastic modulus than $\beta''(Mg_5Si_6)$.

The different strength contributions given in Equation (9) will now be reviewed for the present example, starting with the contribution from dislocations σ_d which is related to the dislocation densities ρ_s and ρ_g through the Taylor equation, i.e., Equation (14). Fig. 10 shows the resulting evolution of these two dislocation densities for the present example of compression-tension loading. It is evident from the figure that these two contributions evolve very differently during the loading cycle. Hence, ρ_s shown in Fig. 10 (a) increases continuously during the complete loading cycle, i.e., both during compression and tension. This is because the evolution of statistically stored dislocations, as given by the Kocks-Mecking equation, is independent of the loading direction. This contrasts with GNDs for which the evolution of ρ_g follows a cyclic evolution during compression-tension loading as shown in Fig. 10 (b). During the initial compression stage, ρ_g increases until a maximum is reached at the transition from compression to tension loading. After the loading direction is reversed, ρ_g starts to decrease until a minimum value is reached at $\varepsilon_p = -0.026$, for which $\rho_g = 0$. This strain corresponds to $\varepsilon_p^* = 0$ in Fig. 9, which is consistent with Equation (16) which states that ρ_g is proportional to $\left|\varepsilon_p^*\right|$. A further increase of the plastic tensile strain beyond $\varepsilon_p = -0.026$ leads to a continuous increase in ρ_g as shown in Fig. 10 (b). Fig. 10 (c) shows the resulting variations of σ_d during the compression-tension loading cycle.

Fig. 11 shows the predicted evolution of the yield stress contribution σ_p during reversed loading, where σ_p corresponds to the overall strengthening effect of particles. When the loading direction is reversed from compression to tension, the non-shearable particles only partially affect the yield strength in the first part of the straining when they are shielded by the dislocation loops. When the unrelaxed plastic strain ε_p^* is zero, and the dislocation loops are annihilated, the non-shearable particles are again fully active in resisting the movement of the dislocations. The overall effect of this change in the interaction between particles and dislocations on σ_p is shown in Fig. 11, where Equation (12) is used with different values of the parameter q for the present example.

In the following, the predictive capability of the kinematic hardening model will be tested by comparison with the measured reverse loading cases that were previously presented. The model is used without any further tuning of parameters, and the only inputs to the model simulations are the chemical composition of the alloy and the temperature and loading histories.

Fig. 12 compares the stress magnitude obtained by calculations and measurements against the accumulated plastic strain for the reversed loading tests for tempers T6, T7 and O. Note that in the calculations with NaMo the pre-compression levels were defined in terms of plastic strain instead of total strain as in the experiments, and thus the simulated pre-compression levels are slightly overestimated. While the calculated curves exhibit a sharp transition between the elastic and plastic domain, the experimental curves display an elastic-plastic transition region typically observed in polycrystalline materials. Despite this difference, it is evident that NaMo captures the overall trends observed in the experiments for all temper conditions and for all pre-compressions shown in Fig. 12.

The different strength contributions to the calculated flow stress evolve differently during a compression-tension cycle as shown in Fig. 13 for the three temper conditions. The curves in this figure correspond to the calculated compression-tension curves in Fig. 12 with a plastic pre-strain in compression of 0.06. Qualitatively, the evolution of the individual strength contributions for the three temper conditions shown in Fig. 13(a), (b) and (c) looks similar. The solid solution strength contribution σ_{ss} remains constant during the entire cycle since this contribution is independent of the loading direction. The backstress σ_b follows the evolution of the unrelaxed plastic strain ε_p^* as expressed by Equation (5). The unrelaxed plastic strain ε_p^* is negative both during the initial pre-compression stage as well as during the first part of the reversed tension cycle, as shown previously in Fig. 10. This is the reason why σ_b remains negative for all temper conditions until the accumulated plastic strain reach about 10%, after which σ_b becomes positive for all temper conditions.

Fig. 13 shows that the dislocation strengthening contribution σ_d has a rather complex evolution during the compression-tension cycle. This is because σ_d is given by Equation (14) as the sum of statistically stored dislocations (SSDs) and geometrically necessary dislocations (GNDs) represented by the dislocation densities ρ_s and ρ_g. As explained previously, these two dislocation densities evolve differently during cyclic loading. ρ_s evolves independently of the loading direction, while ρ_g follows a cyclic evolution. σ_d has a peak value both for the T6 and T7 materials in Fig. 13 (a) and (b) after 0.06 plastic pre-compression. These peak values correspond to maximum values of ρ_g in the transition when the loading direction is reversed. When the accumulated plastic strain p is increased during the following tension cycle, ρ_g starts to decrease until all the GNDs are annihilated and σ_d approach zero and a minimum value, respectively. This corresponds to an accumulated plastic strain p of about 0.10 and 0.09 for the T6 and T7 material in Fig. 13 (a) and (b),

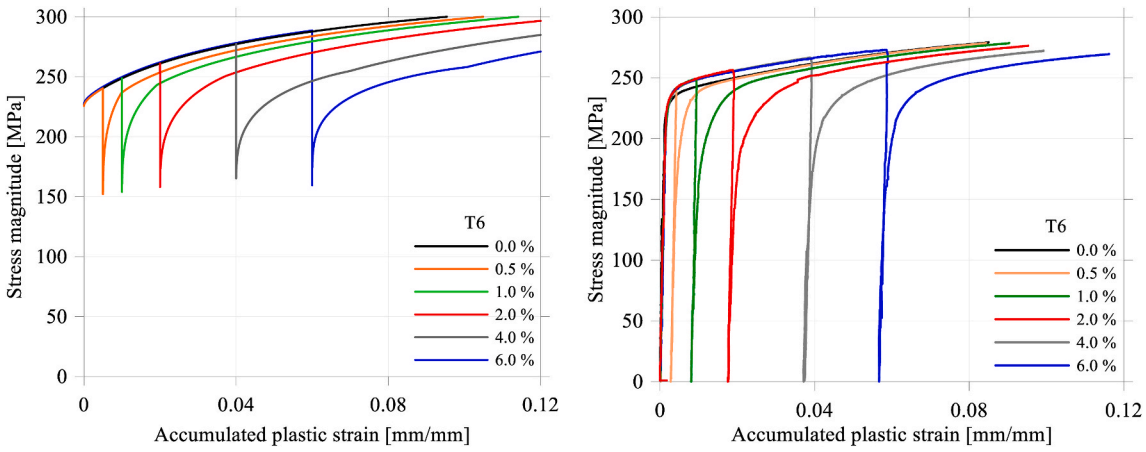

(a)

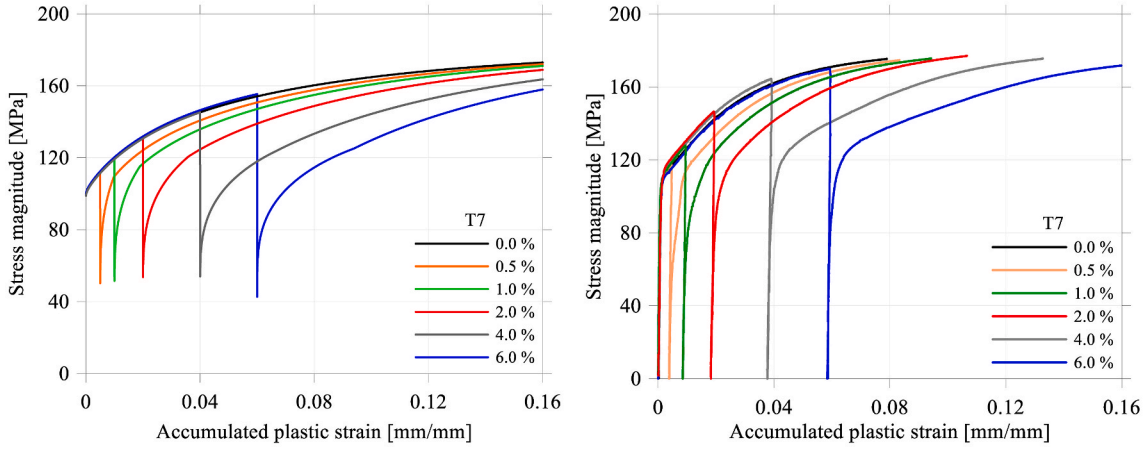

(b)

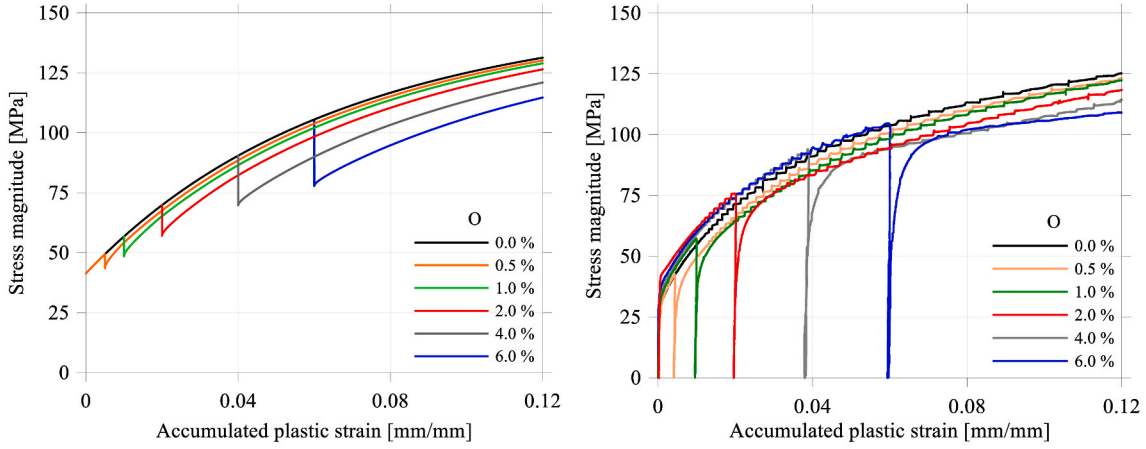

(c)

Fig. 12. Comparison of the stress magnitude against the accumulated plastic strain between calculations (left) and measurements (right) for the reversed loading: (a) Temper T6 (peak strength), (b) Temper T7 (overaged), (c) Temper O (annealed).

respectively. Further plastic straining beyond these plastic strains leads to renewed generation of GNDs followed by an increase of σ_d.

For the O temper material in Fig. 13 (c), the calculated σ_d during the compression-tension cycle is different from the curves for the T6 and T7 materials in Fig. 13 (a) and (b). For this material, σ_d increases steadily with increasing accumulated plastic strain during the whole reversed loading cycle. This is because storing of GNDs during plastic straining is almost negligible for this material due to the precipitate structure characterised by a large geometric slip distance λ_g. As can be seen from Table 4, the calculated λ_g is about 29 μm for the O temper material, while the corresponding magnitudes of λ_g are in turn 0.7 μm and 1.3 μm for the T6 and T7 tempers. Hence, for the O temper material, σ_d is solely dependent on the evolution of SSDs. Since the storing of these

Table 4
Microstructural parameters calculated with NaMo. In addition to the symbols used in Table 3, $\bar{r}$ and λ_g are the mean particle radius and the geometric slip distance, respectively. Concentrations are given in wt% and at% in brackets.

Temper	N_v (#/μm^3)	f	$\bar{r}$ (m)	λ_g (m)	C_{Si}* (wt%)	C_{Mg}* (wt%)
T6	10,800	0.0063	5.18×10^{-9}	7.07×10^{-7}	0.070 (0.067)	0.210 (0.233)
T7	413	0.0068	1.57×10^{-8}	1.26×10^{-6}	0.040 (0.038)	0.190 (0.211)
O	0.13	0.0035	1.85×10^{-7}	2.88×10^{-5}	0.240 (0.230)	0.330 (0.366)

*Based on a simplified assumption in the model of a fixed composition of the particles corresponding to Mg_5Si_6.

dislocations is independent of the loading direction, ρ_s and σ_d increase throughout the entire reversed loading cycle.

From Fig. 13, it is evident that the strength contribution from particles σ_p yields the largest contribution to the overall strength for tempers T6 and T7, while σ_p is small for the O temper condition. The low σ_p for the O temper emerges because the calculated number density N_v of the hardening particles is very low. From Table 4, we find that N_v is only 0.13 #/μm^3 for the O temper, compared with 10,800 #/μm^3 and 413 #/μm^3 for the T6 and T7 tempers, respectively. Fig. 13 shows that σ_p remains constant during the first part of the loading cycle, i.e., during the pre-compression stage which ends at 0.06 plastic strain. When the loading direction is reversed from compression to tension, a significant drop in σ_p for the T6 and T7 materials is seen in Fig. 13 (a) and (b), while the corresponding drop is small but observable also for the O temper material in Fig. 13 (c). As explained previously, the reason for the predicted drop in σ_p when the loading direction is reversed, is because the model assumes that non-shearable particles are initially shielded by dislocation loops when dislocations start moving along the same slip planes but in the opposite direction during reversed loading. In the modelling, the shielding is assumed to be a temporary effect since

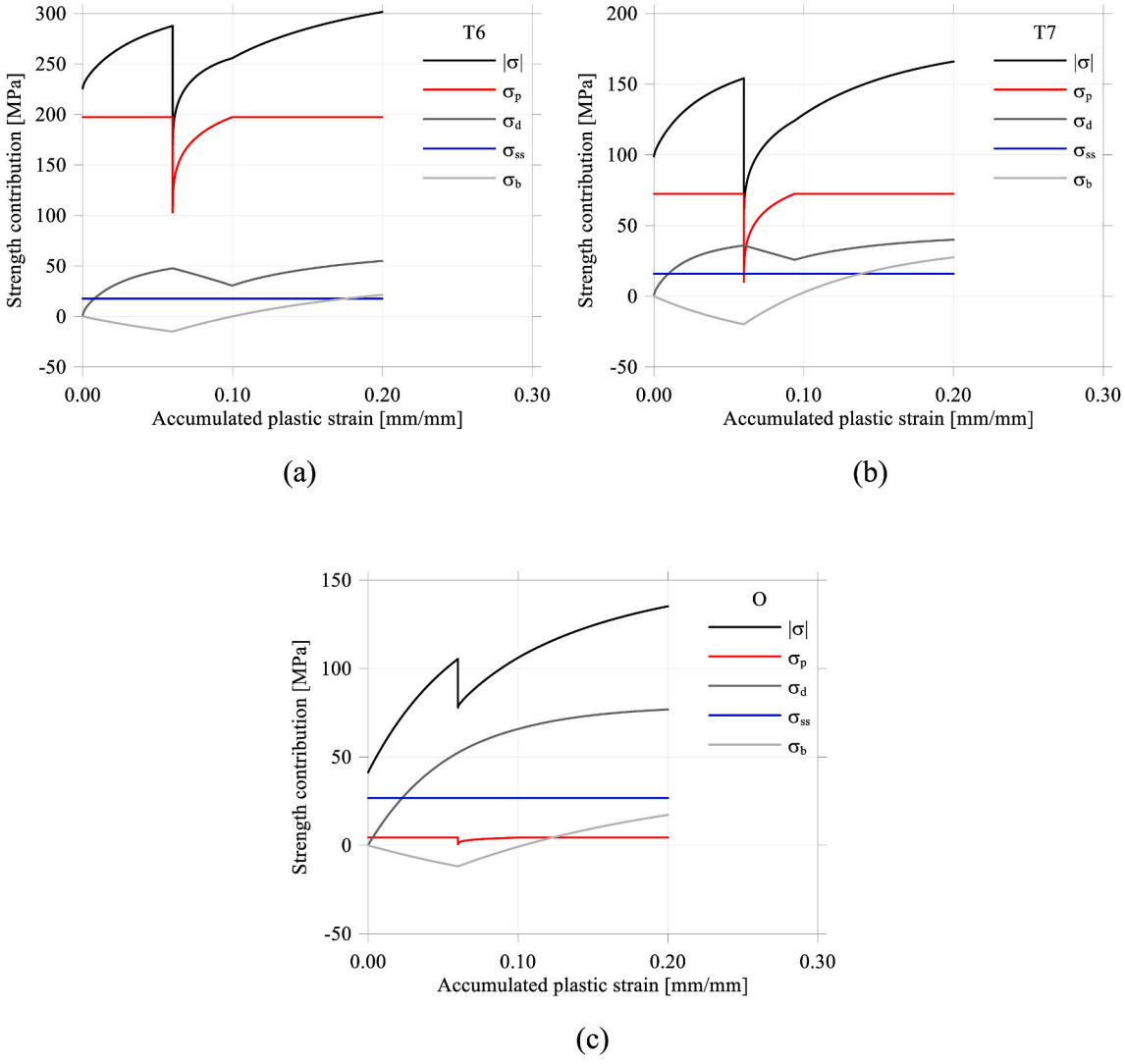

Fig. 13. Calculated stress magnitude and strength contributions as a function of accumulated plastic strain during a compression-tension cycle with a pre-compression of 0.06: (a) temper T6 (peak strength), (b) temper T7 (overaged), (c) temper O (annealed).

prolonged reversed plastic straining eventually leads to complete annihilation of the dislocation loops as the unrelaxed plastic strain ε_p^* approaches zero. At this plastic strain, the non-shearable particles have fully recovered in the sense that they again act as efficient barriers in interactions with dislocations.

6. Concluding remarks

In the present work, kinematic hardening has been incorporated into a nanoscale model for 6000 series aluminium alloys by minor modifications of the mathematical framework of the original isotropic model. This is obtained by assuming that the backstress is caused by an unrelaxed plastic strain around non-shearable particles. In addition, the so-called shielding mechanism that is assumed to operate during reversed loading is introduced in the model. This mechanism can explain the strong Bauschinger effect in the peak aged and overaged conditions that was observed in the experimental compression-tension tests. Since scanning and transmission electron microscopy did not reveal any extensive particle cracking, this mechanism was not included in the present nanoscale model.

The experimental work included compression-tension tests with pre-straining varying from 0.005 to 0.06. Such tests were carried out for a cast and homogenized AA6063 alloy in three different temper conditions, i.e., T6 (peak strength), T7 (overaged) and O (annealed). After calibrating the model with respect to a few parameters related to kinematic hardening, the model was tested for the three tempers and the various pre-straining conditions. In these simulations, the only inputs to the model were the alloy composition, the ageing heat treatment, and the applied loading cycle. It was found that the nanoscale model captured the overall trends observed in the experiments for all temper conditions and pre-compression levels without any tuning from one simulation to the next.

Based on the present work, it is concluded that the nanoscale model with the implemented constitutive relations that enable simulations of kinematic hardening provides a promising tool for different industrial applications where the loading direction is changed during the processing. Possible applications also include simulations of the material response of energy absorbing automotive structural components, as well in simulations of various types of forming operations. The industrial relevance of the nanoscale model is further enhanced since the model is capable of accounting for alloy composition and heat treatment schedules, which are inputs to the model.

CRediT authorship contribution statement

Ole Runar Myhr: Conceptualization, Methodology, Software, Investigation, Writing - original draft. **Tore Børvik:** Conceptualization, Investigation, Visualization, Writing - original draft. **Calin D. Marioara:** Investigation, Writing - original draft. **Sigurd Wenner:** Investigation, Writing - original draft. **Odd Sture Hopperstad:** Conceptualization, Methodology, Writing - original draft.

Declaration of competing interest

The authors declare that they have no known competing financial interests or personal relationships that could have appeared to influence the work reported in this paper.

Acknowledgements

The authors gratefully appreciate the financial support from Norwegian University of Science and Technology (NTNU) and the Research Council of Norway through the FRINATEK Program FractAl, Project No. 250553.

References

Ashby, M.F., 1970. The deformation of plastically non-homogeneous materials. Phil. Mag. 21, 399–424.
Bardel, D., Perez, M., Nelias, D., Dancette, S., Chaudet, P., Massardier, V., 2015. Cyclic behaviour of a 6061 aluminium alloy: coupling precipitation and elastoplastic modelling. Acta Mater. 83, 256–268.
Brown, L.M., Stobbs, W.M., 1971a. The work-hardening of Copper-Silica. I. A model based on internal stresses, with no plastic relaxation. Phil. Mag. 23, 1185–1199.
Brown, L.M., Stobbs, W.M., 1971b. The work-hardening of Copper-Silica. II. The role of plastic relaxation. Phil. Mag. 23, 1201–1233.
Cooper, M., 1967. The crystal structure of the ternary alloy α (AlFeSi). Acta Crystallogr. 23, 1106–1107.
Deschamps, A., Brechet, Y., 1999. Influence of predeformation and aging of an Al-Zn-Mg alloy-II. Modelling of precipitation kinetics and yield stress. Acta Mater. 47, 293–305.
Fourmeau, M., Børvik, T., Benallal, A., Hopperstad, O.S., 2013. Anisotropic failure modes of high-strength aluminium alloy under various stress states. Int. J. Plast. 48, 34–53.
Fribourg, G., Bréchet, Y., Deschamps, A., Simar, A., 2011. Microstructure-based modelling of isotropic and kinematic strain hardening in a precipitation-hardened aluminium alloy. Acta Mater. 59, 3621–3635.
Hasting, H.S., Frøseth, A.G., Andersen, S.J., Vissers, R., Walmsley, J.C., Marioara, C.D., Danoix, F., Lefebvre, W., Holmestad, R., 2009. Composition of β″ precipitates in Al-Mg-Si alloys by atom probe tomography and first principles calculations. J. Appl. Phys. 106, 123527.
Hirsch, J., 2011. Aluminium in innovative light-weight car design. Mater. Trans. 52, 818–824.
Holmen, J.K., Frodal, B.H., Børvik, T., Hopperstad, O.S., 2017. Strength-differential effect in age-hardened aluminium alloys. Int. J. Plast. 99, 144–161.
Kocks, U.F., 1979. Superposition of alloy hardening, strain hardening, and dynamic recovery. In: Proceedings of the 5th International Conference on Strength of Metals and Alloys (ICSMA-5), Aachen, Germany, August 27–31, pp. 1661–1680.
Kocks, U.F., Mecking, H., 2003. Physics and phenomenology of strain hardening: the FCC case. Prog. Mater. Sci. 48, 171–273.
Kristoffersen, M., Børvik, T., Hopperstad, O.S., 2016. Using unit cell simulations to investigate fracture due to compression-tension loading. Eng. Fract. Mech. 162, 269–289.
Lademo, O.G., Engler, O., Benallal, A., Hopperstad, O.S., 2012. Effect of strain rate and dynamic strain ageing on work-hardening for aluminium alloy AA5182-O. Int. J. Mater. Res. 103, 1035–1041.
Langseth, M., Hopperstad, O.S., Berstad, T., 1999. Crashworthiness of aluminium extrusions: validation of numerical simulation, effect of mass ratio and impact velocity. Int. J. Impact Eng. 22, 829–854.
Marioara, C.D., Andersen, S.J., Zandbergen, H.W., Holmestad, R., 2005. The Influence of alloy composition on precipitates of the Al-Mg-Si system. Metall. Mater. Trans. 36A, 691–702.
Myhr, O.R., Grong, Ø., Andersen, S.J., 2001. Modelling of the age hardening behaviour of Al-Mg-Si alloys. Acta Mater. 49, 65–75.
Myhr, O.R., Grong, Ø., Pedersen, K.O., 2010. A combined precipitation, yield strength, and work hardening model for Al-Mg-Si alloys. Metall. Mater. Trans. 41A, 2276–2289.
Myhr, O.R., Grong, Ø., Schäfer, C., 2015. An extended age-hardening model for Al-Mg-Si alloys incorporating the room-temperature storage and cold deformation process stages. Metall. Mater. Trans. 46A, 6018–6039.
Myhr, O.R., Hopperstad, O.S., Børvik, T., 2018. A combined precipitation, yield stress, and work hardening model for Al-Mg-Si alloys incorporating the effects of strain rate and temperature. Metall. Mater. Trans. 49A, 3592–3609.
Pedersen, K.O., Westermann, I., Furu, T., Børvik, T., Hopperstad, O.S., 2015. Influence of microstructure on work-hardening and ductile fracture of aluminium alloys. Mater. Des. 70, 31–44.
Polmear, I., 2005. Light Alloys. From Traditional Alloys to Nanocrystals. Butterworth-Heinemann.
Proudhon, H., Poole, W.J., Wang, X., Bréchet, Y., 2008. The role of internal stresses on the plastic deformation of the Al-Mg-Si-Cu alloy AA6111. Phil. Mag. 88, 621–640.
Qin, J., Holmedal, B., Hopperstad, O.S., 2019. Experimental characterization and modelling of aluminum alloy AA3103 for complex single and double strain-path changes. Int. J. Plast. 112, 158–171.
Rakvåg, K.G., Børvik, T., Hopperstad, O.S., 2014. A numerical study on the deformation and fracture modes of steel projectiles during Taylor bar impact tests. Int. J. Solid Struct. 51, 808–821.
Saito, T., Mørtsell, E.A., Wenner, S., Marioara, C.D., Andersen, S.J., Friis, J., Matsusa, K., Holmestad, R., 2018. Atomic structures of precipitates in Al-Mg-Si alloys with small additions of other elements. Adv. Eng. Mater. 20, 1800125.
Scamans, G., 2018. Electric vehicles spike demand for high strength aluminum extrusions. Lite Metal Age 76, 6–12.
Teichmann, K., Marioara, C.D., Andersen, S.J., Marthinsen, K., 2013. TEM study of β′ precipitate interaction mechanisms with dislocations and β′ interfaces with the aluminium matrix in Al-Mg-Si alloys. Mater. Char. 75, 1–7.
Vissers, R., van Huis, M.A., Jansen, J., Zandbergen, H.W., Marioara, C.D., Andersen, S.J., 2007. The crystal structure of the β′ phase in Al-Mg-Si alloys. Acta Mater. 55, 3815–3823.
Westermann, I., Pedersen, K.O., Furu, T., Børvik, T., Hopperstad, O.S., 2014. Effects of particles and solutes on the strength, work-hardening and ductile fracture of aluminium alloys. Mech. Mater. 79, 58–72.
Yu, R., Zhu, J., Ye, H.Q., 2010. Calculations of single-crystal elastic constants made simple. Comput. Phys. Commun. 181, 671–675.